AGU PUBLICATIONS

JGR

Journal of Geophysical Research: Solid Earth

RESEARCH ARTICLE

10.1002/2013JB010409

Key Points:
- Thrust fault earthquakes are produced in the laboratory
- Both sub-Rayleigh and supershear ruptures are generated and studied
- Surface ground motion signatures are recorded in real time

Correspondence to:
V. Gabuchian,
vgabuchi@caltech.edu

Citation:
Gabuchian, V., A. J. Rosakis, N. Lapusta, and D. D. Oglesby (2014), Experimental investigation of strong ground motion due to thrust fault earthquakes, *J. Geophys. Res. Solid Earth*, *119*, 1316–1336, doi:10.1002/2013JB010409.

Received 6 JUN 2013
Accepted 4 DEC 2013
Accepted article online 17 DEC 2013
Published online 26 FEB 2014

Experimental investigation of strong ground motion due to thrust fault earthquakes

Vahe Gabuchian[1], Ares J. Rosakis[1], Nadia Lapusta[2], and David D. Oglesby[3]

[1]Graduate Aerospace Laboratories, California Institute of Technology, Pasadena, California, USA, [2]Department of Mechanical and Civil Engineering and Seismological Laboratory, California Institute of Technology, Pasadena, California, USA, [3]Department of Earth Sciences, University of California, Riverside, California, USA

Abstract Thrust fault earthquakes are studied in a laboratory earthquake setup previously used to investigate analog strike-slip seismic events. Dynamic mode II ruptures are generated along preexisting faults in an analog material, Homalite H-100, and their interaction with the free surface is studied for both sub-Rayleigh and supershear rupture speeds. High-speed digital photography and laser velocimeter diagnostics are used synergistically to identify and study the ground velocity signatures caused by the various features of the generated ruptures. The obtained surface-normal motions of both sub-Rayleigh and supershear ruptures show substantial asymmetry between the hanging and footwall, with the hanging wall experiencing much larger velocity amplitudes. The main features of the surface velocity traces at various stations can be explained by the calculated arrivals of various waves and fronts—Mach cones, *P* and *S* waves, and sub-Rayleigh features. In both the sub-Rayleigh and supershear cases, the arrival of the rupture tip generates a prominent Rayleigh wave traveling along the simulated Earth's surface. Supershear events feature larger amplitudes of ground shaking profiles. All signatures in the surface motion records attenuate and broaden with increasing distance from the fault trace. The signatures corresponding to the arrival of the Mach fronts attenuate with distance at a slower rate than those from sub-Rayleigh ruptures. The arrival of the updip supershear rupture at the free surface creates a downdip propagating slip feature with its own Mach cone. These additional Mach fronts further amplify ground shaking on the hanging and footwalls.

1. Introduction

The severe effects of several recent thrust earthquakes (e.g., the 1999 $M_w = 7.6$ Chi-Chi earthquake, the 2004 $M_w = 9.2$ Indian Ocean earthquake, the 2008 $M_w = 7.9$ Wenchuan earthquake, and the 2011 $M_w = 9.0$ Tohoku-Oki earthquake) emphasize the special risks that earthquakes on thrust or reverse faults pose: Megathrust faults line the Pacific Rim and intraplate thrust faults lie near many major metropolitan centers around the globe. Furthermore, the tsunamis generated from thrust faults threaten millions of people in fast-growing coastal cities. Therefore, it is crucial to understand the physical behavior of thrust faults, the ground motion they produce, and how these features differ from simpler, more commonly-studied vertical strike-slip faults. There is considerable evidence that dip-slip faults (and thrust faults in particular) display many behaviors that arise from their asymmetric geometry with respect to the Earth's surface. Observational studies [e.g., *Nason*, 1973; *Steinbrugge et al.*, 1975; *Abrahamson and Somerville*, 1996; *Shin and Teng*, 2001] indicate that the ground motion on the hanging wall is typically significantly larger than the ground motion on the footwall. Analog and numerical models of thrust faults [e.g., *Brune*, 1996; *Oglesby et al.*, 1998; *Shi et al.*, 1998; *Oglesby et al.*, 2000; *Ma and Beroza*, 2008] also display this asymmetry in ground motion; it can be partly ascribed to the closer proximity of hanging wall seismic stations to the fault and partly to waves trapped in the hanging wall during fault slips (the latter being shown by asymmetry in the displacements of the two sides of the fault [*Brune*, 1996; *Oglesby et al.*, 1998; *Shi et al.*, 1998]). Furthermore, waves radiated by the updip propagating rupture can reflect from the free surface back onto the fault, leading to time-dependent normal stress on the fault [*Nielsen*, 1998; *Oglesby et al.*, 1998]. This time dependence of normal stress feeds back into the rupture and slip process, leading to amplified near-surface fault motion and near-source ground motion from thrust faults relative to otherwise equivalent normal faults [*Brune*, 1996; *Oglesby and Archuleta*, 1998].

While numerical models may shed a great deal of light on the physical interactions taking place during thrust earthquakes, such models must be compared to real-world observations. For example, *Oglesby and Day* [2001a, 2001b] modeled the dynamics and ground motion of the 1999 Chi-Chi earthquake, and found that a very simple model could explain the significantly higher motion on the hanging wall in this event; the ground motion asymmetry was an inevitable consequence of the dipping fault geometry. Likewise, dynamic models of the 2008 Wenchaun earthquake by *Duan* [2010] correctly reproduce the asymmetric ground motion of this event.

Aside from the fault geometry, another property that can have a strong effect on the ground motion in an earthquake is the rupture velocity—in particular whether the rupture proceeds at a sub-Rayleigh or supershear speed. Although supershear rupture has been surmised as a theoretical possibility [*Burridge*, 1973; *Andrews*, 1976; *Freund*, 1979] and has been inferred in several strike-slip earthquakes, including the 1979 Imperial Valley event [*Archuleta*, 1984], the 2001 Kunlunshan event [*Bouchon and Vallée*, 2003], the 1999 Izmit earthquake [*Bouchon et al.*, 2001, 2002], and the 2002 Denali Fault event [*Ellsworth et al.*, 2004], its frequent occurrence has only recently been widely accepted by the earthquake seismology community. Indeed, it was the experimental discovery of supershear ruptures occurring repeatedly and reproducibly under highly instrumented and controlled laboratory conditions [*Xia et al.*, 2004, 2005; *Lu et al.*, 2009, 2010] that stimulated the recent flurry of theoretical activities on the subject [e.g., *Aagaard and Heaton*, 2004; *Dunham and Archuleta*, 2005; *Liu and Lapusta*, 2008]. It has also motivated seismologists to remove subshear rupture speed restrictions placed on inversions, to revisit a number of historic earthquake events, and to reexamine irregular field observations in search for such a phenomenon [*Song et al.*, 2008]. Supershear rupture can lead to a number of qualitative changes in the near-source ground motion, including a breakup of directivity and a rotation of the peak horizontal ground motion from fault-normal to fault-parallel [*Aagaard and Heaton*, 2004; *Dunham and Bhat*, 2008; *Mello et al.*, 2010]. Supershear rupture propagation has been mostly discussed in the context of strike-slip earthquakes, where the mode II direction susceptible to supershear transition is aligned with the length of the fault. For dip-slip cases, including thrust faults, the mode II direction is aligned with the updip propagation, and supershear propagation and transition in such cases is more difficult to observe even if it occurs. However, even in that case, supershear rupture growth has been suspected in relation to the 2009 $M_w = 6.3$ L'Aquilla earthquake in Italy [*Ellsworth and Chiaraluce*, 2009; *Mello et al.*, 2010]. Hence, it is important to investigate how the unique features of supershear rupture would interact with the asymmetric near-surface geometry of thrust faults.

Even with a growing body of seismological data and numerical models of dip-slip faults, it remains crucial to have more laboratory data obtained by analogue experiments which mimic the dynamics of such faults. Laboratory models help elucidate how important certain features of the numerical models (such as the asymmetry between hanging wall and footwall) are in the real world. They are also the best way to conclusively validate the numerical results, providing the necessary comparisons to physical reality and confidence in predictions made from such models. Perhaps most importantly, though, laboratory experiments are the only way to provide fresh observations of previously unknown phenomenon (discovery) that can then be investigated in numerical models and in seismological data. Indeed, many of the effects of dip-slip faults (i.e., the asymmetry between hanging wall and footwall motion, and amplified motion from thrust faults) noted above were predicted by the analog foam rubber models of *Brune* [1996]. Thus, laboratory experiments, numerical models, and seismic observations can be used together and iteratively to more fully investigate the physics of faulting.

In this study, thrust faults are simulated in a laboratory setting by nucleating a dynamic mode II rupture along a preexisting fault in Homalite H-100, a high-density, transparent polymer. High-speed camera and laser velocimeter diagnostics are used to capture the rupture's propagation toward the surface and the resulting radiated fields and ground motions, following the developments of previous studies (section 2) [e.g., *Xia et al.*, 2005; *Rosakis et al.*, 2007; *Lu et al.*, 2010; *Mello et al.*, 2010]. These diagnostics have been previously utilized to study the ground motions in a strike-slip configuration, bimaterial effects, off-fault damage, and supershear transition length. They provided the first recorded observation of a supershear rupture in the laboratory. In the present study, the experimental setup is modified to facilitate the modeling of thrust faults in two important ways. First, the specimen size has been increased to allow for a sufficient time window of observation on the free specimen edge representing the free surface of the Earth before wave reflections from any other specimen edge arrive there and corrupt the measured response, and second, the

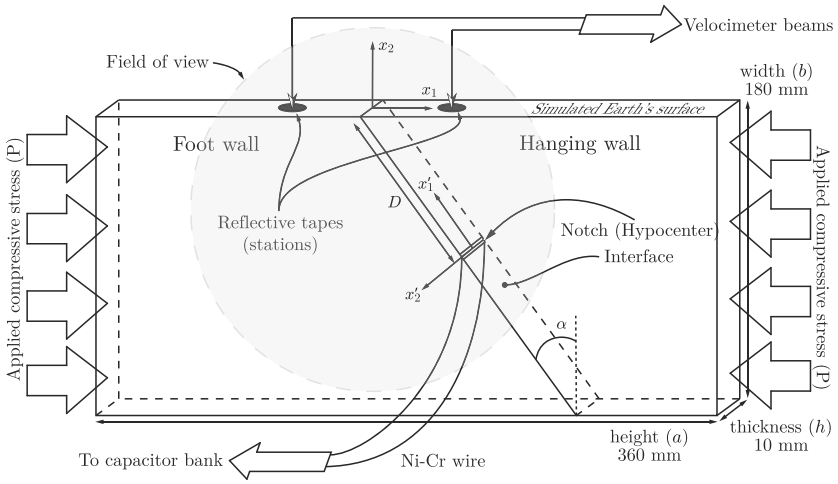

Figure 1. Experimental specimen designed to produce dynamic ruptures on a simulated thrust fault and their interaction with a free surface. The hanging and footwalls of the Homalite specimen are mated along the frictional interface, with one of the specimen edges representing the simulated Earth's surface. Load P results in the resolved normal and shear stress on the interface. The coordinates $x'_1 - x'_2$ are positioned at the hypocenter, with x'_1 directed along the interface. The coordinates $x_1 - x_2$ are linked to the fault trace, with x_1 representing the distance along the simulated Earth's surface. Velocimeter beams are focused onto the reflective tapes and measure the surface-normal (x_2) component of velocity. The field of view illustrates the region captured by the photoelastic images. A Ni-Cr wire is placed between the mating halves at the hypocenter and its explosion is used to initiate the dynamic mode II rupture along the interface. The specimen dimensions are 180 mm × 360 mm.

specimen holder has been redesigned to prevent buckling of the larger samples (Appendix A). We use the developed experimental setup to study the interaction of both subshear and supershear ruptures with the free surface in the context of thrust faults.

2. The Earthquake Visualization Experiment

In our laboratory setup, thrust earthquakes are modeled as dynamic ruptures propagating along a pre-existing fault in a specimen of Homalite H-100, a transparent optically birefringent high-density polymer (Figure 1). The specimens are prepared by taking a Homalite sheet of approximately 10 mm thickness and cutting out rectangles of 180 × 360 mm, dimensions which are set through reflected wave and buckling analyses to avoid reflected waves from the remaining three specimen edges while still being statically stable at higher desired compressive loads. Further details on experimental design can be found in Appendix A. The rectangles are cut at a prescribed interface angle, α, to create two mating pieces. The mating surfaces of the two pieces are polished until an optically reflective surface is obtained, giving a repeatable baseline surface condition from specimen to specimen. The polished interfaces are then bead blasted with glass beads in a repeatable fashion to introduce a uniform and reproducible surface roughness to the interface. To establish a nucleation point and thus a hypocenter for our modeled earthquakes, a square profile notch with the side length of 127 microns is machined through the thickness at a predetermined location along the interface. A Ni-Cr wire is placed in this notch, the two halves are mated, and the specimen is placed in a sample holder, which in turn is placed in a press, where the specimen is slowly preloaded to a compressive stress P. Note that the load is applied vertically in the actual experiments (Figure 2), while the specimen is rotated in Figure 1 to emphasize the analogy with thrust faults.

To trigger dynamic rupture, a capacitor bank (1.5 kV) is discharged across the wire, immediately converting the wire to plasma, and creating a localized pressure release at the interface. The resulting loss of frictional resistive strength allows for the nucleation and initial growth of a mode II rupture, which then spontaneously propagates along the frictional interface (analogous to a fault in the Earth's crust). The discharge of the capacitor also triggers the two diagnostics: high-speed digital photography to capture photoelastic images (contours of maximum shear stress, τ_{max}, *Dally and Riley* [2005]) as well as laser velocimetry to record the Earth's surface-normal ground motions.

Combining two very different outputs—spatially resolved photoelastic images and temporally resolved velocimeter measurements—yields complementary data which can synergistically be used to interpret the

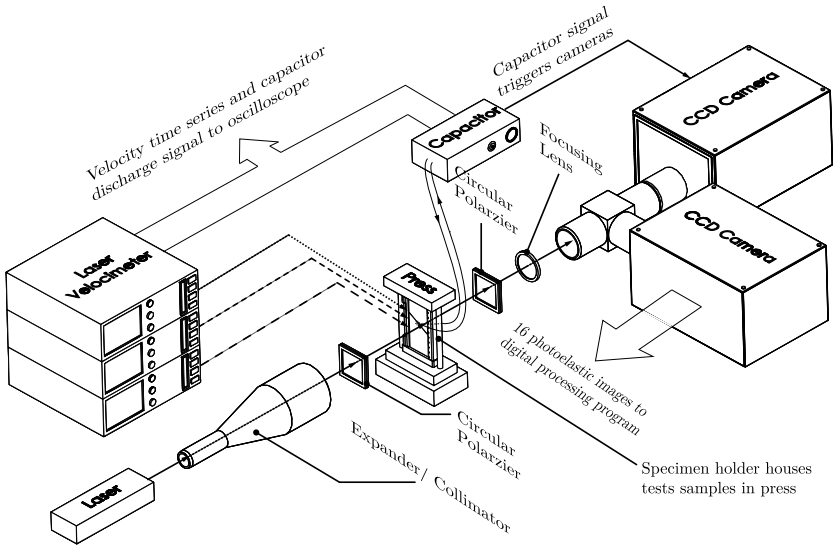

Figure 2. Schematic of the laboratory setup. The deformation of the specimen during dynamic rupture is captured by high-speed cameras in conjunction with photoelasticity. A Verdi V5 green light laser is expanded, collimated, passed through a circular polarizer, the specimen, an oppositely oriented circular polarizer, then focused into the two Cordin Gated-Intensified CCD cameras, which give 16 photoelastic images of the event. Three laser velocimeters are focused onto reflective tapes placed along the simulated Earth's surface (vertical in this view) and record velocity time series. A capacitor bank is discharged across the Ni-Cr wire confined in the notch between the hanging and footwall halves which triggers the camera and velocimeter diagnostics as well as the dynamic event.

dynamic event. Figure 3 is a photograph of the laboratory setup with various views. The light source for photoelastic interferometry is the green light laser beam, which can be seen through its intersection with the various optical components and the specimen. The inserts show the velocimeter heads and the focused red light spots at the measurement locations. More details on the setup and experimental diagnostics are given in *Xia et al.* [2005], *Rosakis et al.* [2007], and *Mello et al.* [2010].

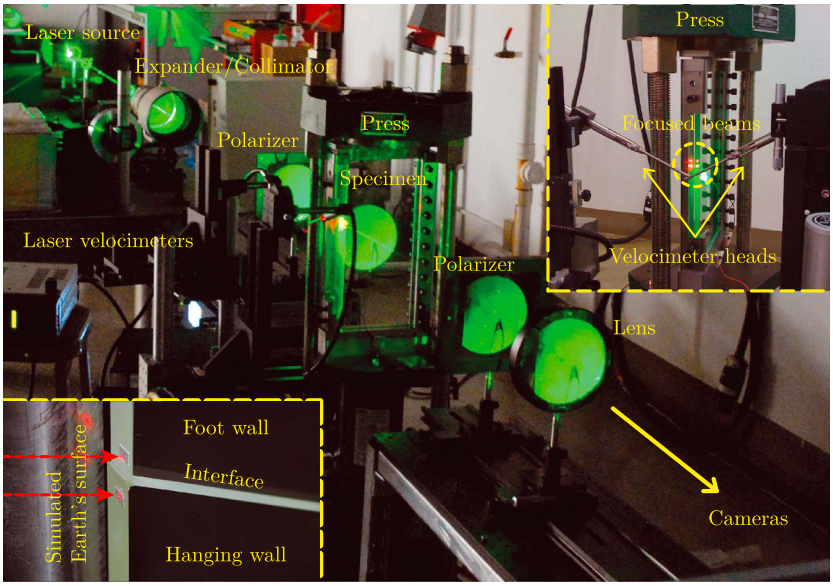

Figure 3. Images of the experimental setup in the lab. The main image shows the laboratory space with the photoelasticity setup, starting at the laser beam output at the top left and ending with the cameras on the bottom right, which capture the collected beam of light. The hydraulic press is to the right of the laser velocimeters and houses the specimen in the sample holder. Top right insert: The velocimeter beams are focused onto the reflective tapes at normal incidence to the simulated Earth's surface. Bottom left insert: The red velocimeter beams are focused onto the reflective tapes on the hanging and footwalls, with a noticeable final postexperiment static displacement at the fault trace.

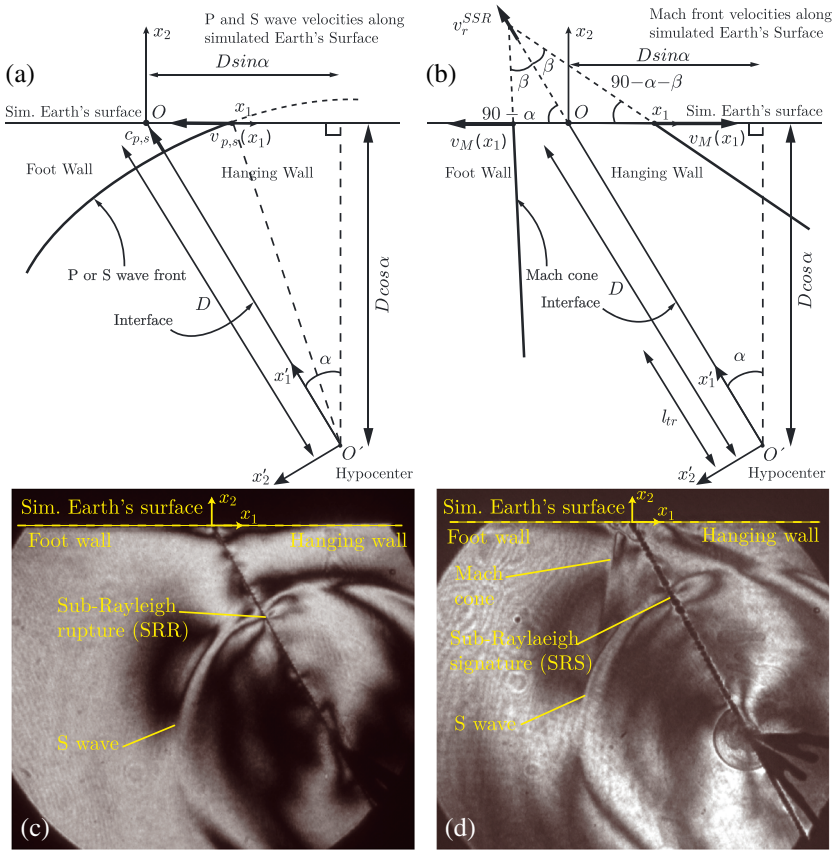

Figure 4. (top) Schematic drawings for analysis of the arrival timing of various features at the simulated Earth's surface, for (left) sub-Rayleigh and (right) supershear ruptures. (bottom) Photoelastic images of a sub-Rayleigh (Figure 4, left) and supershear (Figure 4, right) event. The *P* wave has outrun the *S* wave in both cases and it is absent in both images. The initial *S* wave, the sub-Rayleigh rupture (SRR), the sub-Rayleigh signature (SRS), and the Mach cone are clearly visible. The Mach cone has just arrived at the simulated Earth's surface.

3. Calculation of Feature Arrival Timing

The 16 images from the high-speed cameras with known times allow for determination of speeds of various dynamic features traveling within the specimen. The procedure followed is illustrated in Figure 4. The photoelastic image in Figure 4 (bottom, left) corresponds to a sub-Rayleigh rupture (SRR) moving toward the simulated Earth's surface with a nearly constant speed of $v_r^{\mathrm{SRR}} = 1.13 \pm 0.03$ mm/μs (or 1130 m/s). The sub-Rayleigh rupture tip, identified by a double-lobe fringe pattern, trails just behind the circular *S* wave trace emitted at the time of nucleation. The *S* wave speed is measured directly from the images and found to be $c_s = 1.27 \pm 0.02$ mm/μs. Measurements of the *P* wave speed, $c_p = 2.59 \pm 0.03$ mm/μs, are obtained from earlier images. In later images such as the one in Figure 4, the initial *P* wave front is not visible anymore. The photoelastic image in Figure 4 (bottom, right) corresponds to a rupture which nucleated as sub-Rayleigh and transitioned to supershear speeds, as evidenced by the presence of a Mach cone. In the image, the supershear rupture tip has already reached the simulated Earth's surface and some reflections back downdip are visible. The circular trace of the initial *S* wave, similar to the one present in the sub-Rayleigh rupture image to the left, is also visible. Just behind this circular trace is the stress concentration (double-lobe pattern) traveling upward along the interface, which indicates the sub-Rayleigh signature (SRS). This signature is related to the stresses of the now extinct sub-Rayleigh rupture which transitioned to supershear at an earlier time during the event. This signature has been studied in relation to a strike-slip configuration by *Mello et al.* [2010]. In the experiments where supershear transition is observed, the supershear rupture tip speeds are found to be $v_r^{\mathrm{SSR}} = 2.10 \pm 0.05$ mm/μs. The speed of the sub-Rayleigh signature, however, is always found to be close to the Rayleigh wave speed of Homalite, which is equal to $c_R = 1.18 \pm 0.01$ mm/μs.

To help in identifying the various surface velocity signatures that appear in the velocimeter traces, a geometrical and timing analysis is conducted in order to identify the relative arrivals of the various waves

or Mach fronts incident on the surface and to find the associated propagation speeds of the resulting surface features.

Idealizing the initial *P* and *S* wave fronts as concentric circles originating from the hypocenter, it is clear from Figure 4 (top, left) that these disturbances travel from the hanging wall to the footwall along the simulated Earth's surface, which means that the excitation order of the stations along the hanging wall ($x_1 > 0$) is reversed from that along the footwall ($x_1 < 0$). The arrival times $t_{p,s}(x_1)$ of the *P* and *S* waves to any station x_1 along the simulated Earth's surface can be directly calculated from geometry to be

$$t_{p,s}(x_1) = \frac{D}{c_{p,s}}\sqrt{\left(\sin\alpha - \frac{x_1}{D}\right)^2 + \cos^2\alpha}, \tag{1}$$

where $c_{p,s}$ stands for either *P* or *S* wave speed. Due to the curvature of the *P* and *S* wave fronts, the propagation velocities $v_{p,s}(x_1)$ of the resulting disturbances along the surface are not constant but rather depend on x_1. They are

$$v_{p,s}(x_1) = c_{p,s}\sqrt{1 + \left(\frac{\cos\alpha}{\sin\alpha - x_1/D}\right)^2}. \tag{2}$$

The arrival times $t_{p,s}(x_1)$ and along surface velocities $v_{p,s}(x_1)$ depend on the interface angle α as well as the length *D*, which are characteristics of the fault geometry. If $\alpha = 0°$ (vertical fault), the velocity $v_{p,s} \to \infty$ at station $x_1 = 0$ as expected, since the circular wave front is then tangent to the simulated Earth's surface. For a deep hypocenter ($D \to \infty$) the expression reduces to a simple x_1-independent relation, $v_{p,s} \to c_{p,s}/\sin\alpha$, which is an outcome of increasing the radius of curvature of the wave fronts to infinity and turning the fronts into straight lines.

Similar calculations can be performed for the case of a rupture which has transitioned to supershear speeds, as shown in Figure 4 (right). The appearance of Mach cones is a distinct feature accompanying dynamic supershear ruptures. The rupture tip at the vertex of the Mach cone travels at a speed v_r^{SSR} which satisfies $c_s < v_r^{SSR} < c_p$ [see *Rosakis*, 2002; *Samudrala et al.*, 2002a, 2002b]. The rupture speed is related to the Mach cone angle β through $v_r^{SSR} = c_s/\sin\beta$. Let us idealize the Mach fronts as straight lines which initially appear at a distance l_{tr} from the hypocenter. The distance l_{tr} is called the transition length. The time it takes for the supershear rupture tip (and hence for the Mach cone tip) to arrive at the fault trace ($x_1 = 0$) depends simply on the transition length l_{tr} and the supershear rupture tip speed v^{SSR} as

$$t_M(x_1 = 0) = \frac{l_{tr}}{c_s} + \frac{D - l_{tr}}{v_r^{SSR}}. \tag{3}$$

The time t_M of the arrival of the Mach cone to other locations along the surface are given by

$$t_M(x_1) = t_M(x_1 = 0) + \frac{1}{v_r^{SSR}}\left[\frac{\sqrt{(x_1)^2 - (x_1\sin\alpha)^2}}{\tan\beta} - x_1\sin\alpha\right]. \tag{4}$$

This expression shows that it takes longer for the Mach front to arrive at the footwall stations compared to the symmetrically positioned hanging wall stations, a result also obvious from Figure 4. Since the Mach cones are represented as straight lines, the along surface velocity $v_M(x_1)$ of the Mach cone arrivals is related to the rupture tip speed v_r^{SSR} as

$$v_M(x_1) = v_r^{SSR}\frac{\mathrm{sgn}(x_1)\sin\beta}{\sin\left[90 - \beta - \mathrm{sgn}(x_1)\alpha\right]} = \frac{\mathrm{sgn}(x_1)c_s}{\sin\left[90 - \beta - \mathrm{sgn}(x_1)\alpha\right]}. \tag{5}$$

The expression for $v_M(x_1)$ shows that $v_M(x_1 > 0)$ and $v_M(x_1 < 0)$ are constants with $|v_M(x_1 > 0)| > |v_M(x_1 < 0)|$ and $v_M(x_1 > 0) > 0 > v_M(x_1 < 0)$ for all physically allowed Mach cone angles β. The sign function shows that the order of station excitations is from the nearest to the furthest from the fault trace, on both the hanging and footwalls. This is in contrast to the station excitation order for the *P* and *S* wave disturbances. For the hanging wall, in the case where the sum of angles β and α happen to equal 90°, the velocity $v_M(x_1)$ becomes infinite. This corresponds to the Mach front being parallel to the simulated Earth's surface on the hanging wall. For $\beta \to 90°$ ($v_r^{SRR} \to c_s$), the Mach cone degenerates to a single straight line perpendicular to the frictional interface and traveling toward the simulated Earth's surface at the angle α. In this case, v_M is always negative and there is only one intersection with the free surface.

Finally, the arrival times of the sub-Rayleigh rupture (SRR) front for sub-Rayleigh ruptures and sub-Rayleigh signature (SRS) for supershear ruptures are calculated by dividing the distance D by the experimentally measured speeds and provide a useful timing reference at locations close to the fault trace.

4. Experimental Observations and Their Analysis

In this section, we present results on how supershear and sub-Rayleigh ruptures interact with the simulated Earth's surface. The experiments are used to compare the surface motions on the hanging and footwalls in each of the two rupture speed regimes. The experiments also elucidate the clear differences between surface motion features resulting for sub-Rayleigh versus supershear ruptures. In all the cases, the specimen geometry, including the fault inclination angle $\alpha = 29^\circ$ corresponding to a fault dip of 61°, remain nominally the same. The inclination angle $\alpha = 29^\circ$ is near the limit at which the two plates can statically sustain a load in the uniaxial press setup with the prescribed frictional treatment of the interface. While the 61° dip angle is rather steep for a thrust fault, it is sufficient to illustrate the basic properties of thrust faults (as shown in previous dynamic models, such as *Oglesby and Day* [2001a, 2001b]).

The sub-Rayleigh and supershear ruptures are produced due to different compressive loads P. As discussed in *Andrews* [1976], *Rosakis et al.* [2007], and *Lu et al.* [2007, 2009], the transition length l_{tr} of the rupture to supershear speeds depends on the product of the critical crack length and a function of the seismic ratio, $s = (\tau_s - \tau_0)/(\tau_0 - \tau_d)$, where τ_s and τ_d represent the static and dynamic levels of shear strength in the linear-slip weakening model and τ_0 is the initial shear stress on the fault. Since the critical crack length is inversely proportional to the compression P, keeping all experimental parameters nominally the same and increasing the load predicts shorter transition lengths. Multiple experiments with the same value of P are performed to establish the repeatability of the results and to use the three available velocimeters to measure velocity evolution of different points along the simulated Earth's surface.

4.1. Supershear Thrust Fault Experiments

The compressive load $P = 15$ MPa generates supershear rupture in our experimental setup. The sequence of photoelastic images and velocimeter traces presented in Figures 5 and 6 describes two different experiments performed at nominally the same conditions. In the experiment presented in Figures 5 and 6 (left columns), the three available velocimeters are focused on the hanging wall, at $x_1 = 2$ mm (red trace), $x_1 = 4$ mm (blue trace), and $x_1 = 8$ mm (green trace). In the experiment presented in Figures 5 and 6 (right columns), the velocimeters are focused on the footwall, at $x_1 = -2$ mm (red trace), $x_1 = -4$ mm (blue trace), and $x_1 = -8$ mm (green trace). The shaded bands in the velocimeter trace plots represent the ranges of the theoretically computed arrival times for the P wave (t_p), S wave (t_s), and sub-Rayleigh signature (SRS) at the measurement locations. The finite width of these bands captures arrivals at three different measurement locations (2, 4, and 8 mm). The two sets of photoelastic images represent nominally the same rupture obtained in two experiments with the same conditions and hence can be used to assess the experimental repeatability.

At a time of $t = 40$ μs (Figure 5, top), after the rupture has transitioned to supershear speeds and a Mach cone has formed, the remnants of the sub-Rayleigh rupture tip continue to be visible as the lobe-like fringe pattern trailing behind the S wave front along the interface; we refer to this feature as the sub-Rayleigh signature (SRS). The supershear rupture (SSR) tips propagate bilaterally with the speeds $v_r^{SSR} = 2.05$ mm/μs and $v_r^{SSR} = 2.15$ mm/μs for the experiments with the hanging and footwall measurements, respectively. The transition lengths for the hanging and footwall experiments are $l_{tr} = 29.3$ mm and $l_{tr} = 27.6$ mm, respectively, quite similar values as they should be in these nominally identical experimental setups. The details on computing the transition lengths are given in Appendix B. The P wave, about twice as fast as the S wave, has already disappeared from the field of view. There is a fringe ahead of the rupture tip that corresponds to the dilatational field ahead of the Mach cone [*Mello et al.*, 2010]. As evident from the magnified insert on the velocimeter traces, the P waves have started to arrive at the stations, exciting the hanging wall stations first then sweeping through the footwall stations. The surface-normal velocity from the P waves are minor (on the order of 0.1 m/s).

Soon thereafter ($t = 50$ μs), the rupture tip reaches the simulated Earth's surface (Figure 5, bottom). The dilatational field has swept across all hanging wall stations, with its endpoint marked by the inflections in the hanging wall traces. The Mach fronts have swept across all the hanging wall stations but

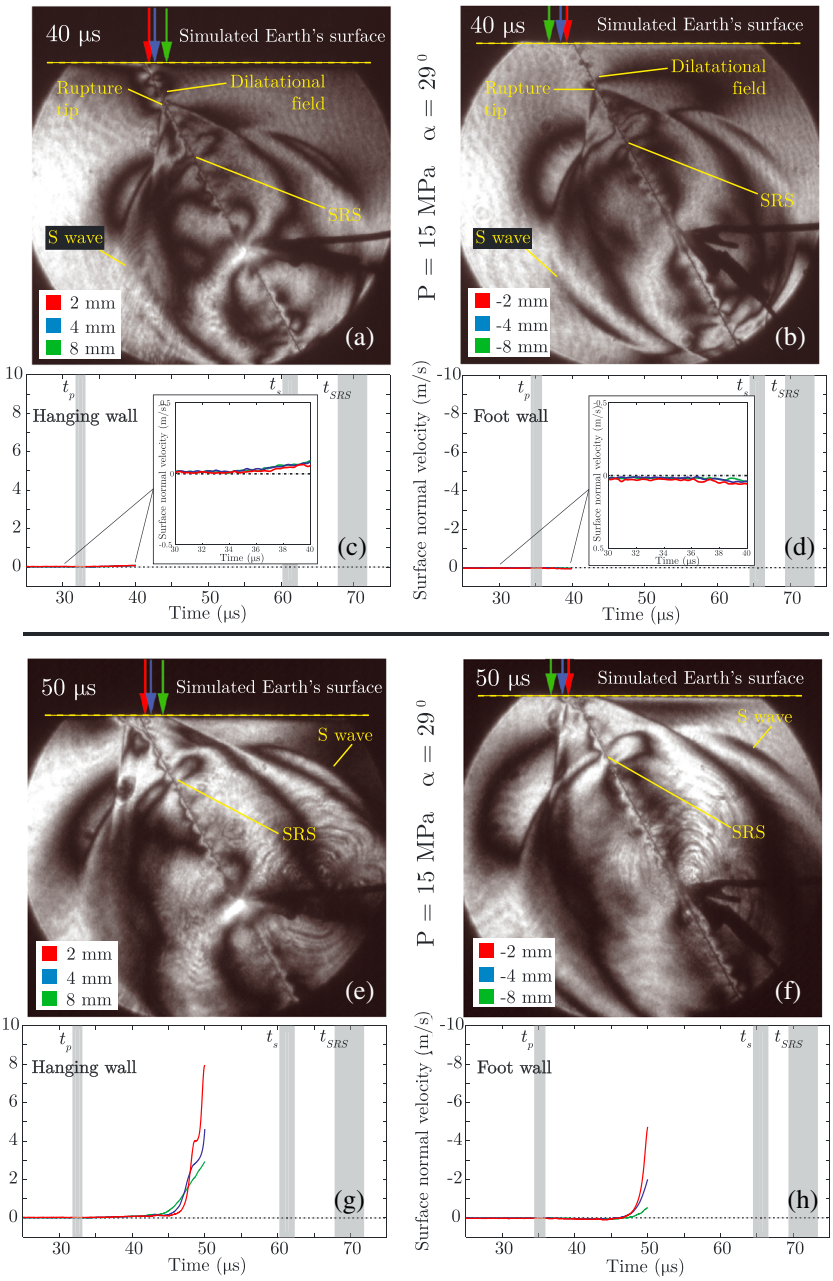

Figure 5. Supershear thrust fault experiments with (top) photoelastic images and (bottom) velocimeter measurements. In each set, (left column) the hanging wall stations located at $x_1 = 2, 4,$ and 8 mm while (right column) the footwall stations located at $x_1 = -2, -4,$ and -8 mm are represented. Timing bands t_p, t_s, and t_{SRS} represent the arrival windows of the initial *P* wave, *S* wave, and the sub-Rayleigh signature to all three stations. For the sake of comparing the surface-normal velocity magnitudes of hanging and footwalls, the footwall velocity axis is reversed. The inserts in Figure 5 (top, left) show that the arrival of *P* waves does induce ground motions, which are difficult to see in the scale of the figures. The yellow lines identify various fringes which correspond to features in the dynamic rupture.

have not yet swept across all footwall stations due to the offset arrival times between hanging and footwalls. The presence of substantial motion at the measurement stations before the arrival of the *S* wave is a clear indication that the dynamic event has indeed transitioned to supershear. The effects of the dilatational field and the Mach fronts are sequentially felt in large surface-normal motions. The hanging wall has an upward motion and the footwall has a downward motion. The arrival of the supershear features has already introduced a large relative velocity between symmetrically placed stations along the hanging and footwalls.

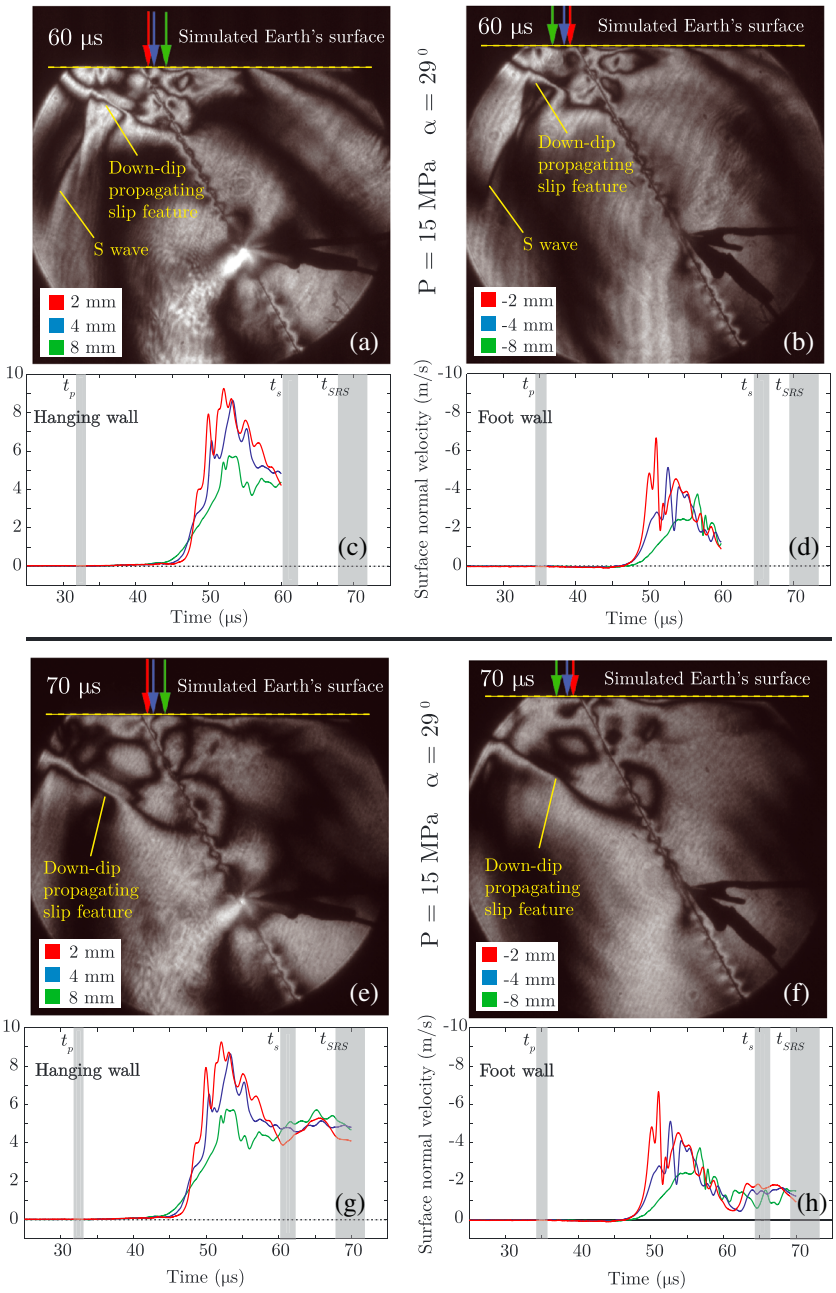

Figure 6. Supershear thrust fault experiments, with (top) photoelastic images and (bottom) velocimeter measurements, continued from Figure 5.

In Figure 6 (top) (t = 60 μs), the effects of the dilatational fields and Mach cones have been sensed throughout the stations. The asymmetry of the ground motions between the hanging and footwalls is enhanced, with the hanging wall stations having larger maximum velocities than those of the corresponding footwall stations. The time to reach the peak of the velocity traces increases with increasing distance from the fault trace, resulting in broader peaks for all given features. The features of the recorded traces are also attenuated with distance from the fault trace, as expected. The photoelastic images show a Mach cone-like feature propagating back downdip, mixing fringes with the incident *S* wave and the trailing SRS; this feature is further discussed in section 4.5. The images also show that the *S* wave is just about to impinge on the furthest station at x_1 = 8 mm.

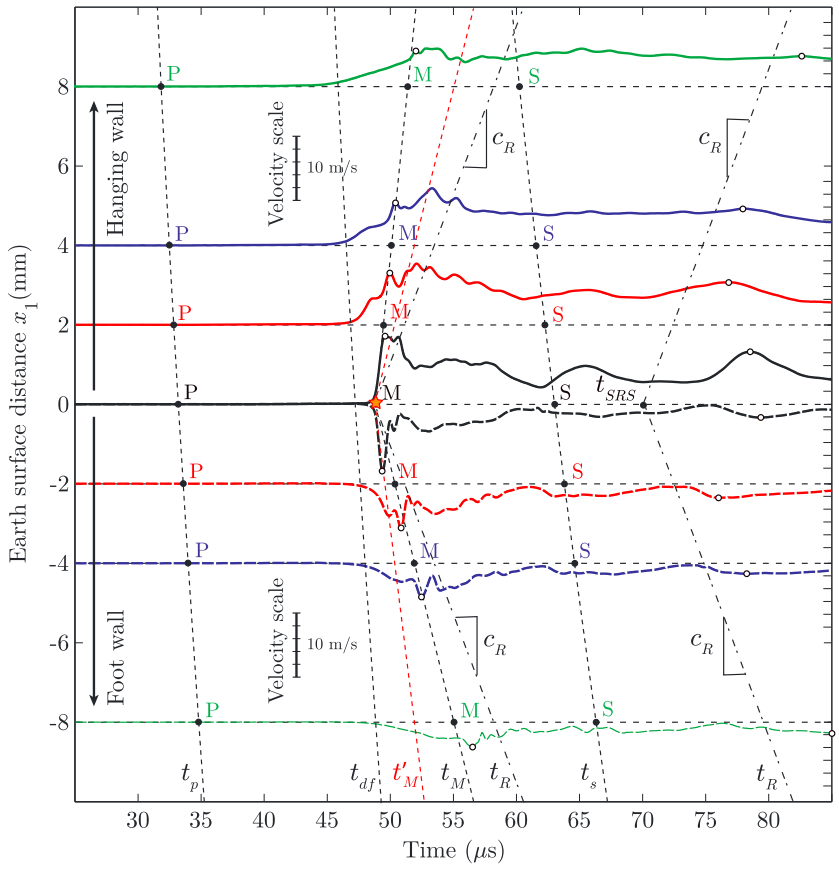

Figure 7. Combined view of velocity measurements at surface stations for supershear experiments, including traces from Figures 5 and 6 (solid and dashed color lines) as well as additional measurements right next to the fault trace, at $x_1 = 0^+$ and $x_1 = 0^-$, done in a separate experiment (black lines). The initial *P* and *S* wave arrival times are given by the dashed black curves labeled t_p and t_s, respectively (equation (1)). The arrival of the incident Mach fronts is given by a pair of dashed black lines labeled t_M (equation (4)). The red dashed lines t'_M represent the arrival of the downdip propagating Mach front discussed in section 4.5. The timing line t_{df} marks the arrival of the rupture tip dilatational field. The arrival of the sub-Rayleigh signature (SRS) at the fault trace, $x_1 = 0$ mm, is marked by the solid circle and labeled t_{SRS} (section 3). A star marks the arrival of the supershear rupture tip to the fault trace, $x_1 = 0$ mm. The dashed lines t_R emanating from the star and the point t_{SRS} mark the timing of Rayleigh-wave disturbances traveling bilaterally along the free surface.

At a later time (Figure 6, bottom, $t = 70$ μs), the Mach cone-like back-propagating feature has traveled more than halfway back downdip toward the hypocenter and the SRS can be identified as the dark-lobed structure just at the fault trace, though it's presence is obscured by the mixing of fringes with the reflected information from the free surface.

To visualize the induced surface motions and their variations, the velocity traces for all measurement stations are plotted in Figure 7. In the time intervals between t_p and t_M, the traces reflect the effects of the initial *P* wave arrival and the following continuous arrivals of *P* waves emitted during the rupture process, including the dilatational field around the Mach cone. The initial *P* wave arrival initiates motion throughout all the stations (not visible on the scale of Figure 7, see insert in Figure 5 (top)). The dilatational field that precedes the Mach cone causes more substantial motion; its arrival is marked by the black dashed line labeled t_{df}.

The rupture tip and the associated Mach fronts reach the stations next (rupture tip marked by a star). The rupture causes strong upward/downward velocities next to the fault trace on the hanging and foot walls, respectively. The Mach fronts arriving at the other stations amplify the effect of the preceding dilatational field. Because of the dip angle asymmetry, the velocities recorded at symmetrically placed stations on the hanging and footwalls are different in magnitude, with the hanging wall having larger velocities than the footwall. As Figure 7 clearly indicates, the calculated times of the Mach cone arrivals correspond remarkably well to the rapid velocity changes in the traces. The velocity maxima for each trace (open circles) shortly follows. Hence, the global maximum for each station is related to the arrival and sweeping of the Mach fronts

across the stations. Note that for some stations ($x_1 = 2$ and $x_1 = 4$), the maximum is achieved after the arrival of the Mach cone, an effect of the free surface and the reflected information propagating back downdip.

The strong arrival of the supershear rupture at the surface is expected to generate surface Rayleigh waves that would start at the fault trace and spread bilaterally across the stations. If we draw the lines marking the projected arrivals of such Rayleigh waves (two dash-dotted lines t_R emanating from the rupture arrival time at the fault trace $x_1 = 0$), we indeed see some relative changes in the traces corresponding to those times. However, these changes are superimposed on all the other effects discussed and hence do not appear very prominently.

Following the ground-shaking signatures associated with the arrival of the dilatational field and the Mach fronts, the traces decrease in magnitude at all stations until the arrival of the *S* wave generated at nucleation. The effect of the *S* wave is to once again increase the ground shaking amplitude as it sweeps the stations. Later, the sub-Rayleigh signature (SRS) arrives at the fault trace, indicated by the black dot marked t_{SRS}. This arrival is also expected to generate Rayleigh waves and their projected arrival at the other stations is marked by two straight dash-dotted lines, $t_R = t_{SRR} + |x_1|/c_R$, emanating from the SRS arrival. Indeed, the velocity traces near the projected arrival times of the Rayleigh wave consistently show an increase of the velocity magnitude. Furthermore, the local maxima of the traces (marked on the traces as the open circles at times larger than 70 μs) seem to propagate with the Rayleigh wave speed along the hanging and footwalls. Note that the dot marked t_{SRS} is positioned based on experiments with measurements at $|x_1| = 2,\ 4,$ and 8 mm, which are consistent for the hanging and footwalls. However, the experiments with the measurements right next to the fault trace has the SRS arrival which is slightly delayed. We attribute this to the shorter transition length of that experiment ($l_{tr} = 22.7$ mm versus the transition lengths of $l_{tr} = 29.3$ mm, and $l_{tr} = 27.6$ mm).

The traces show that the asymmetry of the motions between hanging and footwalls persists throughout the observation window. At the time of 85 μs, all stations on the hanging wall continue to move with the vertical velocity of about 4 m/s. On the footwall, a much smaller velocity amplitude of 1–2 m/s is observed. The substantial difference between the motion on hanging and footwalls is consistent with prior numerical studies [e.g., *Oglesby et al.*, 1998] which attribute the difference to the asymmetry of the fault geometry and the possibility that the wedge-like geometry below the free surface in the hanging wall traps the reflected wave fronts between the free surface and the fault.

After all significant features of dynamic rupture—including the supershear tip, Mach cones, and sub-Rayleigh signature—are done interacting with the free surface within our measurement stations, the motion at the free surface is expected to settle to the near-constant velocity values, at least until artificial reflections arrive from the other specimen boundaries. These near-constant values would be caused by the continuous sliding of the specimen interface behind the sub-Rayleigh signature, as typical for crack-like ruptures. Consistent with this expectation, at the end of the observation window shown in Figure 7, velocities for all the stations on the hanging wall approach a similar value; the same phenomenon occurs on the footwall. Note that the end-of-the-window velocity amplitudes at stations $x = +8$ and $x = -8$ appear to be slightly higher than those at $x = 0^+$ and $x = 0^-$, respectively, but this is because the effects of the Rayleigh waves discussed above has not yet had a chance to decay for the stations farthest from the fault trace. Since stations closer to the fault trace have higher peak amplitudes, the near-constant velocities at the end of the observation window imply that the amplitude decays more for stations closer to the fault trace. It is also interesting to see that the behavior of points closer to the fault trace is richer and more "dynamic," with higher amplitudes alternating with near-zero values, indicating back-and-forth motions, while the stations further away from the fault move with near-constant amplitudes. This is, perhaps, to be expected, as rupture features interact more strongly with the points closer to the fault trace.

4.2. Sub-Rayleigh Thrust Fault Experiments

Decreasing the load from $P = 15$ MPa to $P = 5$ MPa results in sub-Rayleigh events [*Rosakis et al.*, 2007; *Lu et al.*, 2009, 2010]. As predicted by theoretical calculations of l_{tr}, it is possible to have a supershear transition with $P = 5$ MPa; however, this does not occur in the experiments because the interface length D is shorter than the estimates on l_{tr}, and a sub-Rayleigh rupture is observed for the entire duration of the experiment. The photoelastic images in the case of a sub-Rayleigh rupture are of the type shown in Figure 4 (bottom, left). A collection of the surface motion measurements analogous to the supershear case of Figure 7 is presented in Figure 8.

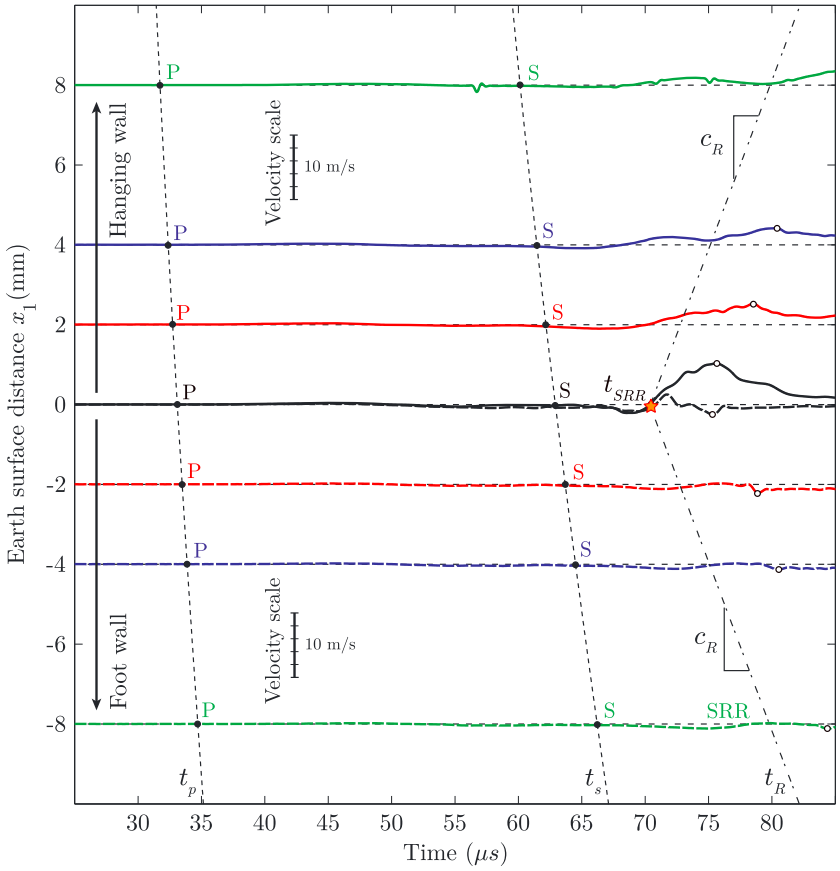

Figure 8. Combined view of velocity measurements at surface stations for three sub-Rayleigh experiments with an applied load of $P = 5$ MPa. A total of three nominally identical experiments with velocimeter data obtained from stations $x_1 = -8, -4, -2, 0^-, 0^+, +2, +4,$ and $+8$ mm are shown. The two black traces at $x_1 = 0^-$ and 0^+ mm correspond to a single experiment, with two velocimeters measuring the surface-normal motion just to the right and left of the fault trace ($x_1 = 0^+$ and $x_1 = 0^-$, respectively). The initial *P* and *S* wave arrival times are given by the dashed curves labeled t_p and t_s, respectively (equation (1)). The arrival of the sub-Rayleigh rupture (SRR) at the fault trace, $x_1 = 0$ mm, is marked by a star labeled $t_{SRR} = D/v_r^{SRR}$. The dashed lines t_R emanating from the star mark the timing of a Rayleigh disturbance traveling bilaterally along the free surface.

It is observed that unlike in the supershear case, the free surface experiences very little motion in the time periods between the t_p and t_s lines. The order of magnitude of these minor motions is 0.1 m/s, as shown in the bottom of Figure 9.

Following the arrival of the *S* waves, all stations experience a small but noticeable increase of the velocity magnitude, of the order of 1 m/s. It is only after the arrival of the sub-Rayleigh rupture tip at the fault trace (black curves) that larger ground velocities are observed, first at $x_1 = 0^+$ mm and $x_1 = 0^-$ mm locations, and subsequently at other stations. In other words, when the SRR tip arrives at the fault trace, significant surface disturbances are generated and then spread bilaterally along the free surface, with the speed approximately equal to c_R.

4.3. Experimental Reproducibility

The question of reproducibility of different, yet nominally identical, experiments needs to be addressed in every experimental data set where comparisons are made across such different experiments (e.g., Figure 7). Figure 9 (top) displays a collection of three nominally identical experiments corresponding to the far-field load $P = 15$ MPa and angle $\alpha = 29°$. In all of these experiments, transition of the rupture to supershear has been observed through dynamic photoelasticity. Figure 9 (bottom) displays a second set of three nominally identical experiments for which the far-field load is $P = 5$ MPa while the angle is kept at $\alpha = 29°$. The ruptures in these three cases remained sub-Rayleigh.

We see that the experimental results are quite repeatable. In the three supershear experiments, Mach front peaks are well-aligned and arrive at the theoretically estimated time t_M. As already discussed in relation

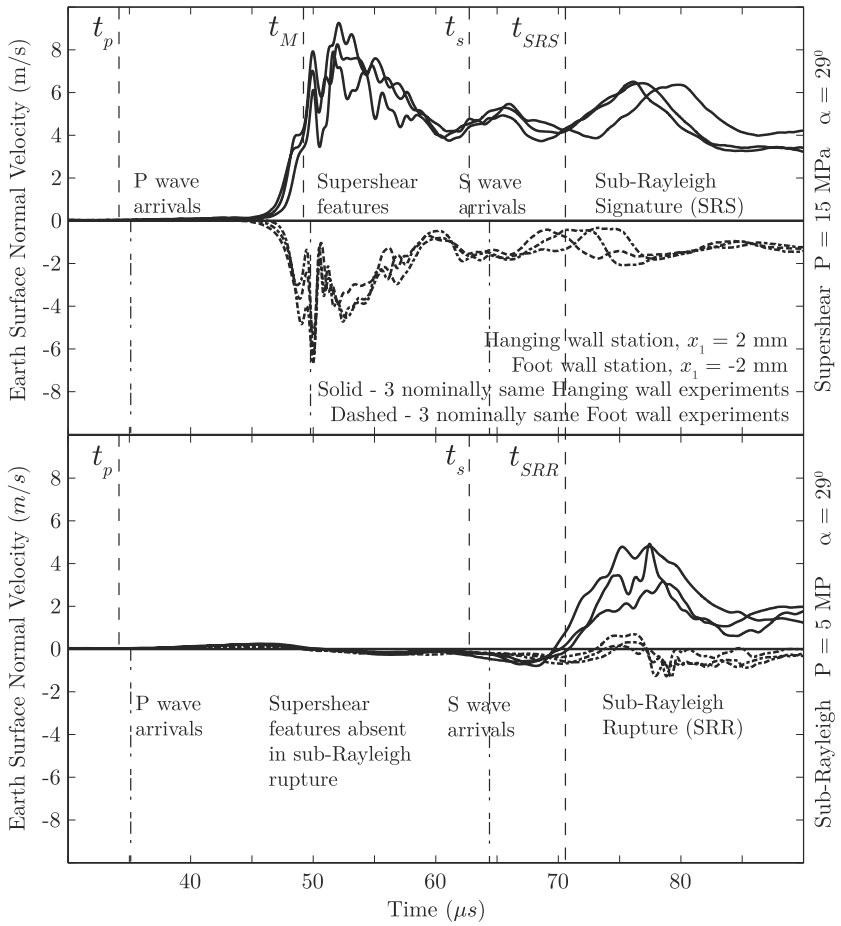

Figure 9. Experimental reproducibility illustrated through velocimeter traces measured at a symmetric distance $|x_1| = 2$ mm on the hanging walls (solid) and footwalls (dashed), for (top) supershear and (bottom) sub-Rayleigh experiments. The experiments have nominally the same conditions, with the sub-Rayleigh set conducted at a load of $P = 5$ MPa and the supershear set at $P = 15$ MPa. The pairs of vertical lines t_p, t_M, t_s, and t_{SRS} (or t_{SRR}) indicate the arrivals of the initial *P* wave, Mach fronts, initial *S* wave, and the sub-Rayleigh signature (or the sub-Rayleigh rupture tip) to the stations at the hanging and footwall plates.

to Figure 7, the arrival times t_s of the *S* wave result in a local amplitude increase, as does the arrival of the effect associated with the trailing sub-Rayleigh signature. The amplitudes of all traces are remarkably similar throughout the duration of the recordings for both hanging and footwalls. The only significant difference between the experiments is in the arrival times of the maxima following t_{SRS}. We attribute these time differences to small variations of the transition length calculated from the photoelastic images. The transition lengths of the three experiments are 29.3 mm, 27.6 mm, and 22.7 mm. The experiment with the transition length of 22.7 mm results in the largest time delay between the Mach peak and the SRS peak. As numerically shown by *Lu et al.* [2009], the transition length is very sensitive to the frictional parameters of the interface as well as the exact nucleation conditions, and we attribute the measured differences in the transition distance to small variations in surface preparation and nucleation conditions.

Figure 9 (bottom) compares three sub-Rayleigh experiments. A small upswing in all traces is first observed just after the arrival of the *P* wave at times t_p. Just after the arrival of the *S* waves, a small downswing is observed while the major ground shaking only becomes evident after the time t_{SRR} when the sub-Rayleigh rupture reaches the fault trace. Note that in this particular experiment, the rupture tip propagates at $v_r^{SRR} = 1.14$ mm/μs, nearly at the Rayleigh wave speed of Homalite, $c_R = 1.18 \pm 0.03$ mm/μs. The three experiments exhibit similarities in the timing of feature arrivals and the wavelengths of various signatures. The variation in amplitudes is likely due to the same reasons as given for the supershear experiments, namely small variations in surface preparation and nucleation procedure.

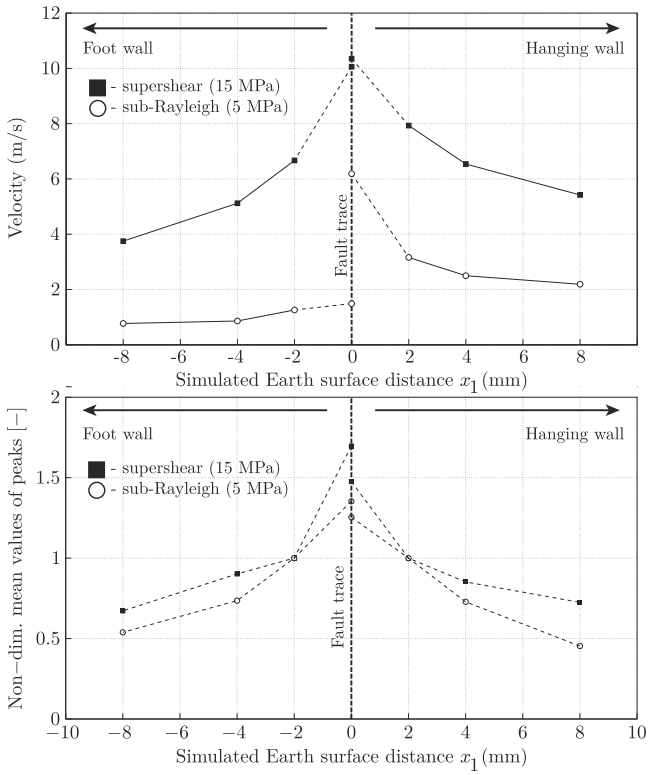

Figure 10. Attenuation of the maxima of surface measurements in supershear experiments (solid squares) and in the sub-Rayleigh experiments (open circles) with distances away from the fault trace. (top) Measurements from a total of six experiments. Each solid line represents one experiment with stations located at $|x_1| = 2, 4$, and 8 mm. The other two experiments, one supershear and one sub-Rayleigh, focus the velocimeters on $x_1 = 0^+$ and $x_1 = 0^-$ and their results are connected to the other data sets with dashed lines. (bottom) Mean value of maxima from all experiments, nondimensionalized by each set's mean value at distance $|x_1| = 2$ mm. The SRR peaks attenuate faster than M peaks outside of $|x_1| = 2$.

4.4. Comparison of Sub-Rayleigh and Supershear Ground Shaking Signatures

As discussed in sections 4.1 and 4.2, there are obvious qualitative differences in the surface motion records corresponding to the supershear and the sub-Rayleigh set of experiments (e.g., Figures 7 and 8). Here, we compare the absolute maximum vertical velocity values at various stations for the six experiments (Figure 10). The solid squares represent peak values for supershear ruptures while the open circles represent peak values for sub-Rayleigh ruptures. Figure 10 (bottom) plots the mean values of each peak set from all experiments, nondimensionalized by the mean value of the set at a distance of $|x_1| = 2$ mm from the fault trace.

At the fault trace, the supershear experiments feature maximum surface velocities of about 10 m/s on both hanging and footwalls. However, the surface velocities for sub-Rayleigh experiments are about 6 m/s on the hanging wall and only 1.5 m/s on the footwall, exhibiting much higher asymmetry. Higher stresses and hence higher stress drops in the supershear experiments explains the observation of overall higher levels of surface velocity, as also observed by *Mello et al.* [2010]. The maximum surface velocity magnitudes for the supershear experiments at the fault trace are just at the instrument saturation level of 10 m/s for the laser velocimeter systems. Though the peak widths for the hanging and footwall traces at the saturation level of 10 m/s are 0.46 μs and 0.10 μs, respectively, suggesting that the signals have nearly peaked, these points are unreliable for use in the attenuation study. The sub-Rayleigh results for peak vertical velocity are qualitatively quite comparable to the numerical models of *Duan and Oglesby* [2005] (Figure 8).

For measurements at $|x_1| = 2, 4$, and 8 mm stations (solid lines), the peak values of supershear cases attenuate slower than the peak values of sub-Rayleigh cases, as expected due to slower decay of motion along Mach fronts [*Mello et al.*, 2010]. Within a distance $|x_1| \leq 2$ mm, it appears that peaks for supershear experiments attenuate faster, however, the measurements on the fault trace are from different experiments and are also near the saturation level of the instruments and hence, this conclusion is not reliable.

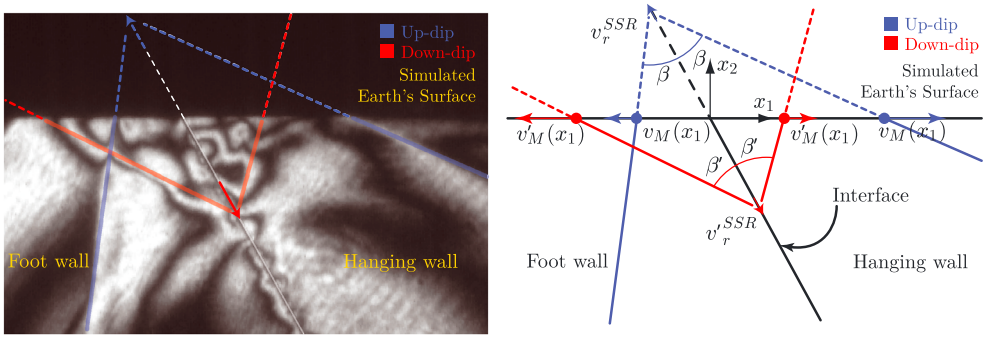

Figure 11. The downdip propagating Mach front is captured in the (left) enlarged photoelastic and (right) schematically illustrated images. The fringes from the downdip propagating slip feature are clearly visible in the footwall plate, but are obscured in the hanging wall plate. The photoelastic image shows that on the hanging wall, the incident Mach front arrives earlier to any given station on the Earth's surface than the complex fringe pattern from the downdip propagating slip feature. The situation, however, is reversed for the footwall, as a fringe travels ahead of the updip Mach front to any given station on the footwall plate.

4.5. Downdip Propagating Features

An interesting finding from the photoelastic images is a clear Mach cone propagating back downdip after the supershear rupture tip has reached the fault trace, as can be seen in the supershear image/trace sequence of Figures 5 and 6. This downdip propagating Mach front is readily seen on the footwall, but obscured on the hanging wall because of reflected radiation and the associated complex photoelastic fringe pattern (Figure 11).

The downdip propagating Mach cone must be associated with a rupture tip-like radiating feature propagating back toward the hypocenter. Note that the interface is likely still slipping while the feature propagates over it, as evidenced by continuing relative motion on the two sides of the fault trace (Figure 6, bottom). Hence, the feature is not, strictly speaking, a rupture tip, since it does not separate slipping and locked areas.

The photoelastic images are used to determine the angle of the downdip propagating Mach front with respect to the interface (β' in Figure 11) and hence the associated rupture speed. Based on the footwall images, the average downdip rupture speed is $\overline{v'^{SSR}_r} = 2.45$ mm/μs. This is $\sim 17\%$ greater than the incident SSR speed of $v_r^{SSR} = 2.10$ mm/μs. Note that some parts of the Mach front appear curved in the later images (Figure 6); however, the entire assembly of fringes moves down at supershear speeds. The curved nature of the Mach front may be a consequence of complex superposition of the incident updip rupture and the downdip propagating disturbance.

To see whether the arrival of the downdip propagating Mach cone affects the surface motion, a timing analysis is done similar to the one in section 3, using the schematic in Figure 11 (right). Assuming that the downdip propagating slip feature is generated at the same instant as the incident Mach cone hits the fault trace, a simple change $x_1 \rightarrow -x_1$ and $\beta \rightarrow \beta'$ in equations (4) and (5) gives the arrival timing, $t'_M(x_1)$, of the downdip propagating Mach fronts to any station x_1 on the simulated Earth's surface as well as the along surface disturbance velocity, $v'_M(x_1)$. Note that on the footwall, the signature of the downdip slip feature travels ahead of, and faster than, the incident Mach front. In contrast, on the hanging wall, the signature of the downdip slip feature travels behind, and slower than, the incident Mach front.

On the surface of both walls, the theoretically predicted arrival times of the downdip propagating Mach cone match the beginning of surface velocity increase (Figure 7, red dashed lines marked t'_M). On the hanging wall, this effect is added to the preceding effect of the incident Mach front, resulting in the global maximum for the traces at $x_1 = 2$ mm and $x_1 = 4$ mm. The signatures of the downdip propagating Mach cone on the footwall is less pronounced, as it is mixed with the effect of the dilatational field that precedes the rupture.

5. Conclusions

The laboratory setup has been redesigned to study the near-fault trace ground motions of a simulated thrust fault. The redesigned and optimized experimental setup has allowed us to study experimentally obtained ground motion records of a thrust fault configuration for both sub-Rayleigh and supershear ruptures with an uncorrupted observation window of up to 110 μs.

The obtained surface-normal motions of both sub-Rayleigh and supershear ruptures show substantial asymmetry between the hanging wall and the footwall, with the hanging wall experiencing much larger velocity amplitudes. This finding is consistent with both field observations [e.g., *Nason*, 1973; *Steinbrugge et al.*, 1975; *Abrahamson and Somerville*, 1996; *Shin and Teng*, 2001] and numerical models [*Oglesby et al.*, 1998; *Shi et al.*, 1998; *Oglesby et al.*, 2000; *Ma and Beroza*, 2008]. The asymmetry is likely due to the trapped waves in the hanging wall [e.g., *Oglesby et al.*, 1998].

The main features of the surface velocity traces at various stations can be explained by the arrivals of various waves and fronts, as expected from the timing analysis. In both the sub-Rayleigh and supershear cases, the global maxima of vertical ground motion velocities occur right at the fault intersection with the free surface (fault trace) and are caused by the arrival of the rupture tip. The arrival of both the supershear rupture tip and sub-Rayleigh signature, as well as the arrival of the sub-Rayleigh rupture tip in the subshear case, generates a noticeable signature traveling bidirectionally along the simulated Earth's surface with the Rayleigh wave speed, suggesting that a Rayleigh wave is generated at the fault trace. The presence of a strong Rayleigh wave radiated by the breakout of rupture to the surface matches the kinematic models of *Madariaga* [2003]. In the supershear case, both the arrivals of the main Mach front and the reflected supershear information result in velocity increases in the off-fault trace locations, with the peak velocities for the off-fault traces caused by either the main Mach front or the reflected information following shortly after.

All arriving signatures attenuate and broaden with increasing distance from the fault trace. The signatures corresponding to the arrival of the Mach fronts are expected to attenuate with distance at a slower rate than the signatures from the sub-Rayleigh rupture. This is indeed observed for surface stations which are located at $|x_1| = 2$ mm from the fault trace and farther. In the sub-Rayleigh case, the fault trace peak velocity magnitudes show a large asymmetry (6 m/s on the hanging wall versus 1.5 m/s on the footwall). Such extreme asymmetry in the vertical ground motion seen in the sub-Rayleigh case right at the fault trace may have been observed in the 1971 San Fernando quake, in which an asphalt road surface may have been flipped into the air right on the toe of the hanging wall [*Allen et al.*, 1998]. The results for the sub-Rayleigh case are also quite consistent with vertical motion in numerical models such as *Duan and Oglesby* [2005]. The fault trace peak velocity magnitudes for the supershear case are just at the limit of the instrument capabilities; thus, these points are unreliable and though the records seem to be reaching their peaks, no conclusion can be made about the hanging and footwall asymmetry. The nature of the attenuation right next to the fault trace would need to be further studied in future experiments.

Another interesting finding is the generation of the downdip propagating slip disturbance in the supershear case which creates its own Mach cone-like features. The downdip supershear slip is generated when the updip incident rupture tip strikes the free surface at the fault trace. The resulting additional Mach cone gives rise to additional peaks in the surface velocity traces, increasing the peak surface velocities. These peaks arrive before those generated by the main, updip Mach cones for the stations on the footwall, and after the main Mach cone peaks on the hanging wall, creating additional complexity in the traces. The downdip rupture speed estimated from the Mach cone angle and its tip advancement is 17% greater than the incident updip supershear rupture tip speed, potentially reflecting the difference in frictional properties and stress conditions encountered by the two ruptures. The experimental observation of the secondary downdip propagating slip disturbance is significant for earthquake source inversions, where it is often assumed that each fault point slips only during the propagation away from the hypocenter, and special source time functions are used to encapsulate that assumption. If a secondary delayed slip feature travels along the fault in the opposite direction, as suggested by our experiments, the presence of that feature would not be uncovered by such earthquake source inversion methods.

Overall, our study has confirmed the expected asymmetry between the hanging and footwall motions, while identifying significant differences between the interaction with the free surface of a sub-Rayleigh versus supershear rupture.

Appendix A: Determination of the Sufficient Specimen Size by Reflected Wave and Buckling Analyses

One of the experimental goals is to measure the motion velocities at the simulated Earth's surface as well as the fault motion caused by waves reflected off of the simulated free surface. Waves reflected off the

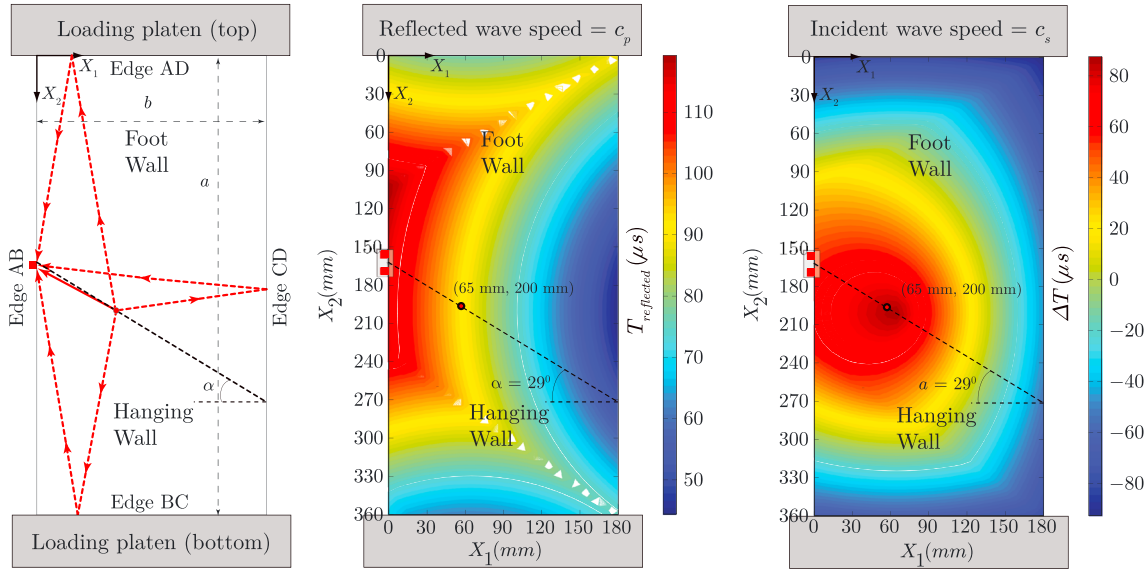

Figure A1. Calculation of unwanted reflected wave arrivals to ensure sufficient observation windows. (left) The minimum paths of travel for unwanted reflected waves originating at the hypocenter are illustrated for a surface location. (middle) Arrival time of the first unwanted reflected waves to each point of the specimen for the chosen specimen size of 180 mm × 360 mm. It allows for an uncorrupted observation window of $T_{\text{reflected}} \sim 110$ μs for stations a distance up to 50 mm away from the fault trace. (right) The value of $\Delta T = T_{\text{reflected}} - T_{\text{incident}}$ is given, which is the difference between the first reflected wave arrival and the incident S wave arrival to any specimen location.

specimen edges other than the simulated Earth's surface are eventually expected to corrupt the measured signals in the sense that such boundaries are absent for natural faults.

The measurement at the simulated Earth's surface must record the effects of the incident waves from the rupture propagating toward the surface (Figure A1), as well as continuing motion after rupture reaches the surface, before the reflected waves arrive from the loading platens and the opposite specimen boundary. In previous studies, the specimen size was 150 mm × 150 mm, with the hypocenter in the middle of the specimen. For sub-Rayleigh ruptures, the travel time to the simulated Earth's surface would be ∼ 70 μs. The reflection from the loading platens of the *P* waves emitted during nucleation would arrive at the intersection of the fault with the surface at about the same time, potentially corrupting the measurement there. Our goal is to avoid such potential contamination in the experiments of this study. Note that *P* and *S* wave speeds in Homalite are $c_s = 1.27$ and $c_p = 2.59$ mm/μs, respectively.

Hence, a numerical calculation is performed to determine a combination of plate width, plate height, and the hypocenter location which will give sufficient uncorrupted measurement time at the locations of interest. The specimen design is bound by several additional constraints. The loading platens on the press must be greater than the width of the specimen to assure uniform loading conditions thus, limiting the width of the specimen to 180 mm. The height is limited by potential buckling of the specimen under the applied loads. It is also desired to have the interface length *D* from the hypocenter to the fault trace of ∼ 70 mm or more, to allow for rupture development and supershear transition in some cases, based on previous studies by *Xia et al.* [2004], *Liu and Lapusta* [2008], and *Lu et al.* [2009]. For each point of the specimen, we consider all possible wave paths for reflected waves originally emitted from the hypocenter at the beginning of the experiment. Examples of such paths for a point at the simulated Earth's surface and each of potentially problematic boundaries are given in Figure A1 (left). The minimum arrival time of reflections over all such paths is then determined. This time, denoted by $T_{\text{reflected}}$, can be computed for both *P* waves and *S* waves. The computation for *P* waves gives the experimental observation window uncorrupted by reflections. However, since the amplitudes of *P* waves are much smaller than those of *S* waves, the computation based on *S* waves indicates the potentially acceptable observation window (which would be about twice longer).

By testing various plate dimensions and hypocenter locations, the following specimen design was selected. The specimen dimensions are 180 mm × 360 mm, with the hypocenter placed at the location of $(X_1, X_2) = (65, 200)$ mm measured from the upper left corner in Figure A1. This results in *P* wave-based $T_{\text{reflected}}$ of 110 μs or more at the near-fault stations, i.e., within 50 mm of the fault trace (Figure A1, middle). (In the panel,

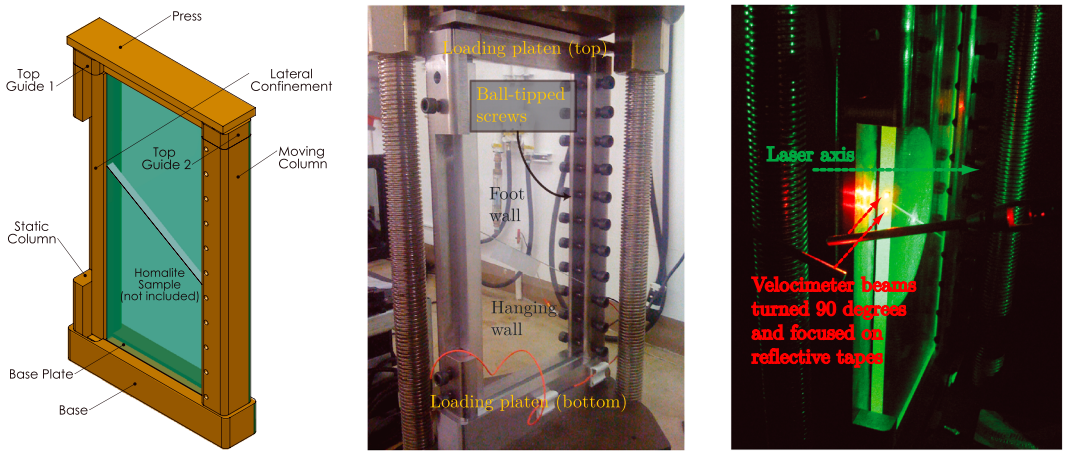

Figure A2. The experimental design driven by avoiding unwanted reflected waves and buckling limits of the material. To prevent buckling, the specimen edge opposite to the simulated free surface needs to be supported, according to a buckling analysis. To implement such support, a linear array of ball-tipped screws is integrated into the specimen holder design. (left) An isometric view of the specimen holder with threaded holes to accommodate the ball-tipped screws spread in a linear array along the part labeled *Moving Column*. (middle) The Homalite specimen loaded into the holder and placed in the press where load P is applied. The *Lateral Confinement* column remains in the holder to stabilize the specimen only during initial loading. (right) The *Lateral Confinement* column is removed to expose the experimental free surface. The expanded and collimated laser light passes through the specimen, defining the field of view, and the red velocimeter beams are focused onto reflective tapes located on the specimen.

the red circle marks the hypocenter location and the line at the angle of $\alpha = 29°$ represents the frictional interface.) This is sufficient for observations, as shown in Figure A1 (right), which plots the difference ΔT between the uncorrupted observation window $T_{\text{reflected}}$ and the arrival time of the first S wave, T_{incident}. This time period is the duration of the signal of interest at any point in the sample.

A buckling analysis of the enlarged plate is conducted to assure that the experimental specimen will not buckle under the compressive loads ($P \sim 15$ MPa) needed for the ruptures to transition to supershear speeds. For the specimen design of previous studies [*Lu et al.*, 2009], in which two specimen edges (other than the loading edges) are free surfaces, the critical load for buckling on the current large specimen is $\sigma_{\text{crit}} = 13.5$ MPa. This is below the desired operating loads of 15 MPa. It is known from plate theory [*Timoshenko and Gere*, 2010] that the critical buckling load increases with increased constraints on the system. Hence, our solution is to change one of the specimen edges from free to simply-supported, as seen in Figure A2, which restricts out-of-plane motions. This alteration results in a critical buckling load of $\sigma_{\text{crit}} = 18.5$ MPa.

The simply-supported boundary condition for one of the edges is implemented in the specimen holder design by placing a linear array of ball-tipped screws along one column of the specimen holder, as seen in Figure A2. These ball-tipped screws permit in-plane motion while restricting out-of-plane motion, and cannot carry a moment about the axis of the linear array. This is an accurate representation of the modified simply-supported boundary condition which yields a higher critical buckling load. The ball-tipped screws stabilize the specimen while being minimally intrusive to the rupture dynamics: regardless of the boundary conditions of this edge, the reflected wave calculations assure that information from this surface will not corrupt the signal for the desired experimental time window of 110 μs. Indeed, the specimen does not buckle for applied loads of $P = 15$ MPa used to generate the supershear experiments presented in the following sections.

Appendix B: Computing Transition Length l_{tr} From Photoelastic Images

Photoelastic images provide information about the transition lengths of supershear ruptures. However, it is difficult to capture an image where the rupture is exactly at the transition point. The following derives a method to estimate the transition length given an image at a time T_1 after the time of transition, T_0, where $T_1 > T_0$. Performing this calculation for every image captured after transition and averaging the results gives an estimate of transition length.

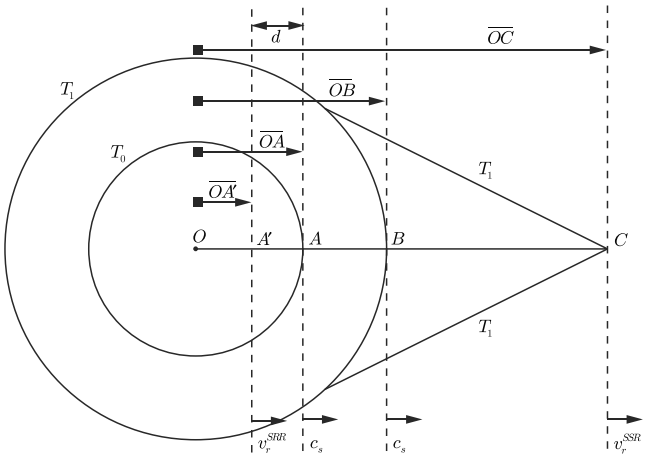

Figure B1. Determination of transition length l_{tr} through photoelastic images. The supershear event is drawn at two different times, one at time T_0 where the transition occurs and at a later time in the event, T_1. The transition distance, l_{tr}, is equal to the length $\overline{OA}$ or $\overline{OA'}$, depending on the physical mechanism of transition, the discrepancy between the two mechanisms being the small distance d on the order of several millimeters.

The geometry in Figure B1 sets up the problem. Two shear wave fronts, one at time T_0 and the other at T_1, are moving with the *S* wave speed, c_s. At the time T_1, the rupture has already transitioned to supershear speeds; hence, Mach cones are present as shown in Figure B1. The supershear rupture tip at time T_1 is at *C*. The rupture tip speed prior to transition is given by v_r^{SRR} and the rupture speed after transition is given by v_r^{SSR}. The derivation uses the various lengths defined in Figure B1 to solve for the time, T_0, when transition occurs. Multiplying T_0 by an appropriate speed yields the transition length l_{tr}. Two cases of transition locations are considered following two physical mechanisms for transition.

B1. Case I: Transition Occurs at Pileup of Shear Waves

In the first mechanism, it is assumed that transition happens as described by the Burridge-Andrews mechanism [*Andrews*, 1976; *Rosakis*, 2002]. In this mechanism, the pileup of shear waves just ahead of the sub-Rayleigh main crack becomes strong enough to nucleate a daughter rupture ahead of the original sub-Rayleigh rupture. The new rupture is born supershear (at point A in Figure B1) and marks the transition onset irrespective of the current location of the sub-Rayleigh main rupture. The length $\overline{BC}$ is used to determine the time of transition T_0 as

$$\overline{BC} = (v_r^{SSR} - c_s)(T_1 - T_0), \tag{B1}$$

$$T_0 = T_1 - \left(\frac{\overline{BC}}{v_r^{SSR} - c_s}\right). \tag{B2}$$

To obtain the transition length, T_0 must be multiplied by the wave speed of point *A* giving the transition length as

$$l_{tr} = c_s\left[T_1 - \left(\frac{\overline{BC}}{v_r^{SSR} - c_s}\right)\right]. \tag{B3}$$

In actual experiments, one measures $\overline{OB}$ and $\overline{OC}$ to get $\overline{BC}$ as $\overline{BC} = \overline{OC} - \overline{OB}$.

B2. Case II: Transition Occurs Directly at the Sub-Rayleigh Rupture Tip

The case of direct transition of an originally sub-Rayleigh rupture to supershear, at the rupture tip, was analyzed in the numerical investigation of *Liu and Lapusta* [2008]. This transition occurs behind the shear wave front; thus, introducing a new length, *d*. We have

$$\overline{OA'} = v_r^{SRR} T_0, \tag{B4}$$

$$\overline{A'C} == v_r^{SSR}(T_1 - T_0), \tag{B5}$$

$$\overline{OC} = v_r^{SSR}(T_1 - T_0) + v_r^{SRR}T_0. \tag{B6}$$

Taking the difference between $\overline{OC}$ and $\overline{OB}$ and solving for T_0 gives

$$\overline{BC} = \overline{OC} - \overline{OB} = v_r^{SSR}T_1 - v_r^{SSR}T_0 - c_sT_1 + v_r^{SRR}T_0 \tag{B7}$$

$$T_0 = T_1\left(\frac{v_r^{SSR} - c_s}{v_r^{SSR} - v_r^{SRR}}\right) - \left(\frac{\overline{BC}}{v_r^{SSR} - v_r^{SRR}}\right). \tag{B8}$$

To obtain the transition length $l_{tr} = \overline{0A'}$, T_0 must be multiplied by v_r^{SRR}

$$l_{tr} = v_r^{SRR}\left[T_1\left(\frac{v_r^{SSR} - c_s}{v_r^{SSR} - v_r^{SRR}}\right) - \left(\frac{\overline{BC}}{v_r^{SSR} - v_r^{SRR}}\right)\right]. \tag{B9}$$

Comparison of equations (B3) and (B9) shows that for practical purposes, these two analyses give very similar transition lengths. This is because the rupture tip speed, v_r^{SRR}, is typically around c_R which is close to c_s. Once the transition length is determined (or the value T_0), the distance d can be estimated as

$$d = T_0(c_s - v_r^{SRR}) \tag{B10}$$

and gives values of the order of $d = 3 - 6$ mm. From the available photoelastic images it is not possible to distinguish between case I and case II. Hence, in this work, we use case I to compute l_{tr}.

Acknowledgments
This study was supported by the National Science Foundation (grant EAR 1142183) and the Southern California Earthquake Center (SCEC). SCEC is funded by NSF Cooperative Agreement EAR-0529922 and U.S. Geological Survey Cooperative Agreement 07HQAG0008. The SCEC contribution number for this paper is 1767.

References

Aagaard, B. T., and T. H. Heaton (2004), Near-source ground motions from simulations of sustained intersonic and supersonic fault ruptures, *Bull. Seismol. Soc. Am.*, *94*, 2064–2078.

Abrahamson, N. A., and P. G. Somerville (1996), Effects of the hanging wall and footwall on ground motions recorded during the Northridge earthquake, *Bull. Seismol. Soc. Am.*, *86*, 93–99.

Allen, C. R., J. N. Brune, L. S. Cluff, and A. G. Barrows (1998), Evidence for unusually strong near-field ground motion on the hanging wall of the San Fernando fault during the 1971 earthquake, *Seismol. Res. Lett.*, *69*, 524–531, doi:10.1785/gssrl.69.6.524.

Andrews, D. J. (1976), Rupture velocity of plane strain shear cracks, *J. Geophys. Res.*, *81*, 5679–5687, doi:10.1029/JB081i032p05679.

Archuleta, R. J. (1984), A faulting model for the 1979 Imperial Valley earthquake, *J. Geophys. Res.*, *89*(B6), 4550–4585, doi:10.1029/JB089iB06p04559.

Bouchon, M., and M. Vallée (2003), Observation of long supershear rupture during the magnitude 8.1 Kunlunshan earthquake, *Science*, *301*, 824–826, doi:10.1126/science.1086832.

Bouchon, M., M.-P. Bouin, H. Karabulut, M. N. Toksoz, M. Dietrich, and A. J. Rosakis (2001), How fast is rupture during an earthquake? New insights from the 1999 Turkey earthquakes, *Geophys. Res. Lett.*, *28*, 2723–2726, doi:10.1029/2001GL013112.

Bouchon, M., M. N. Toksoz, H. Karabulut, M.-P. Bouin, M. Dietrich, M. Aktar, and M. Edie (2002), Space and time evolution of rupture and faulting during the 1999 Izmit (Turkey) earthquake, *Bull. Seismol. Soc. Am.*, *92*, 256–266, doi:10.1785/0120000845.

Brune, J. N. (1996), Particle motions in a physical model of shallow angle thrust faulting, *Proc. Indian Acad. Sci.*, *105*, 197–206.

Burridge, R. (1973), Admissible speeds for plane-strain self-similar shear cracks with friction but lacking cohesion, *Geophys. J. R. Astron. Soc.*, *35*, 439–455, doi:10.1111/j.1365-246X.1973.tb00608.x.

Dally, J., and W. Riley (2005), *Experimental Stress Analysis*, 4th ed., College House Enterprises, Knoxville, Tenn.

Duan, B. (2010), Role of initial stress rotations in rupture dynamics and ground motion: A case study with implications for the Wenchuan earthquake, *J. Geophys. Res.*, *115*, B05301, doi:10.1029/2009JB006750.

Duan, B., and D. D. Oglesby (2005), The dynamics of thrust and normal faults over multiple earthquake cycles: Effects of dipping fault geometry, *Bull. Seismol. Soc. Am.*, *95*, 1623–1636, doi:10.1785/0120040234.

Dunham, E. M., and R. J. Archuleta (2005), Near-source ground motion from steady state dynamic rupture pulses, *Geophys. Res. Lett.*, *32*, L03302, doi:10.1029/2004GL021793.

Dunham, E. M., and H. S. Bhat (2008), Attenuation of radiated ground motion and stresses from three-dimensional supershear ruptures, *J. Geophys. Res.*, *113*, B08319, doi:10.1029/2007JB005182.

Ellsworth, W. L., and L. Chiaraluce (2009), Supershear during nucleation of the 2009 m 6.3 L'Aquila, Italy earthquake, *Eos Trans. AGU*, *90*(52), Fall Meet. Suppl., Abstract U13C-07.

Ellsworth, W. L., M. Celebi, J. R. Evans, E. G. Jensen, D. J. Nyman, and P. Spudich (2004), Processing and modeling of the Pump Station 10 record from the November 3, 2003, Denali fault, Alaska earthquake, paper presented at 11th International Conference on Soil Dynamics and Earthquake Engineering, vol. 1, pp. 471–477, Berkeley, Calif.

Freund, L. B. (1979), The mechanics of dynamic shear crack propagation, *J. Geophys. Res.*, *84*(B5), 2199–2209.

Liu, Y., and N. Lapusta (2008), Transition of mode II cracks from sub-Rayleigh to intersonic speeds in the presence of favorable heterogeneity, *J. Mech. Phys. Solids*, *56*, 25–50, doi:10.1016/j.jmps.2007.06.005.

Lu, X., N. Lapusta, and A. J. Rosakis (2007), Pulse-like and crack-like ruptures in experiments mimicking crustal earthquakes, *Proc. Natl. Acad. Sci. U.S.A.*, *104*(48), 18,931–18,936, doi:10.1073/pnas.0704268104.

Lu, X., N. Lapusta, and A. J. Rosakis (2009), Analysis of supershear transition regimes in rupture experiments: The effect of nucleation conditions and friction parameters, *Geophys. J. Int.*, *177*, 717–732, doi:10.1111/j.1365-246X.2009.04091.x.

Lu, X., A. J. Rosakis, and N. Lapusta (2010), Rupture modes in laboratory earthquakes: Effect of fault prestress and nucleation conditions, *J. Geophys. Res.*, *115*, B12302, doi:10.1029/2009JB006833.

Ma, S., and G. C. Beroza (2008), Rupture dynamics on a bimaterial interface for dipping faults, *Bull. Seismol. Soc. Am.*, *98*(4), 1642–1658, doi:10.1785/0120070201.

Madariaga, R. (2003), Radiation from a finite reverse fault in a half space, *Pure Appl. Geophys.*, *160*, 555–577.
Mello, M., H. S. Bhat, A. J. Rosakis, and H. Kanamori (2010), Identifying the unique ground motion signatures of supershear earthquakes: Theory and experiments, *Tectonophysics*, *493*, 297–326.
Nason, R. (1973), Increased seismic shaking above a thrust fault, in *San Fernando, California, Earthquake of February 9, 1971, Geol. and Geophys. Stud.*, vol. 3, edited by N. A. Benfer, J. L. Coffman, and J. R. Bernick, pp. 123–126, Natl. Oceanic and Atmos. Admin., Washington, D. C.
Nielsen, S. B. (1998), Free surface effects on the propagation of dynamic rupture, *Geophys. Res. Lett.*, *25*, 125–128, doi:10.1029/97GL03445.
Oglesby, D. D., and S. M. Day (2001a), Fault geometry and the dynamics of the 1999 Chi-Chi (Taiwan) earthquake, *Bull. Seismol. Soc. Am.*, *91*, 1099–1111.
Oglesby, D. D., and S. M. Day (2001b), The effect of fault geometry on the 1999 Chi-Chi (Taiwan) earthquake, *Geophys. Res. Lett.*, *28*, 1831–1834, doi:10.1029/2000GL012043.
Oglesby, D. D., R. J. Archuleta, and S. B. Nielsen (1998), Earthquakes on dipping faults: The effects of broken symmetry, *Science*, *280*, 1055–1059, doi:10.1126/science.280.5366.1055.
Oglesby, D. D., R. J. Archuleta, and S. B. Nielsen (2000), The three-dimensional dynamics of dipping faults, *Bull. Seismol. Soc. Am.*, *90*, 616–628, doi:10.1785/0119990113.
Rosakis, A. J. (2002), Intersonic shear cracks and fault ruptures, *Adv. Phys.*, *51*, 1189–1257, doi:10.1080/00018730210122328.
Rosakis, A. J., G. Lykotrafitis, K. Xia, and H. Kanamori (2007), Dynamic shear rupture in frictional interfaces: Speeds, directionality, and modes, in *Treatise in Geophysics, Earthquake Seismol.*, vol. 4, edited by G. Schubert and H. Kanamori, Elsevier, New York.
Samudrala, O., Y. Huang, and A. J. Rosakis (2002a), Subsonic and intersonic mode II crack propagation with a rate-dependent cohesive zone, *J. Mech. Phys. Solids*, *50*, 1231–1268, doi:10.1016/S0022-5096(01)00129-6.
Samudrala, O., Y. Huang, and A. J. Rosakis (2002b), Subsonic and intersonic shear rupture of weak planes with a velocity weakening cohesive zone, *J. Geophys. Res.*, *107*(B8), 2170, doi:10.1029/2001JB000460.
Shi, B., A. Anooshehpoor, J. N. Brune, and Y. Zeng (1998), Dynamics of thrust faulting: 2D lattice model, *Bull. Seismol. Soc. Am.*, *88*, 1484–1494.
Shin, T.-C., and T.-L. Teng (2001), An overview of the 1999 Chi-Chi, Taiwan, earthquake, *Bull. Seismol. Soc. Am.*, *91*(5), 895–913, doi:10.1785/0120000738.
Song, S. G., G. Beroza, and P. Segall (2008), A unified source model for the 1906 San Francisco earthquake, *Bull. Seismol. Soc. Am.*, *98*(2), 823–831.
Steinbrugge, K. V., E. E. Schader, and D. F. Moran (1975), Building damage in San Fernando Valley, in *San Fernando, California, Earthquake of 9 February 1971*, *Bulletin 196*, chap. 25, edited by G. B. Oakeshott, pp. 323–353, Calif. Div. of Mines and Geol., Sacramento, Calif.
Timoshenko, S. P., and J. M. Gere (2010), *Theory of Elastic Stability*, 2nd ed., pp. 360–370, McGraw Hill International Editions, New York, NY.
Xia, K., A. J. Rosakis, and H. Kanamori (2004), Laboratory earthquakes: The sub-Rayleigh-to-supershear rupture transition, *Science*, *303*, 1859–1861, doi:10.1126/science.1094022.
Xia, K., A. J. Rosakis, and H. Kanamori (2005), Supershear and sub-Rayleigh-intersonic transition observed in laboratory earthquake experiments, *Exp. Tech.*, *29*, 63–66.